# RESEARCH ARTICLE

# Analytical methods for the geometric optics of thermal vision illustrated with four species of pitvipers

George S. Bakken[1,*], Samantha E. Colayori[1,†] and Taihung Duong[2]

[1]Department of Biology, Indiana State University, Terre Haute, IN 47809, USA and [2]Indiana University School of Medicine at Terre Haute, Terre Haute, IN 47809, USA

*Author for correspondence (george.bakken@indstate.edu)
†Present address: Department of Pharmacology and Physiology, University of Rochester, Rochester, NY 14642, USA

## SUMMARY

**The pitviper facial pit is a pinhole camera-like sensory organ consisting of a flask-shaped cavity divided into two chambers by a suspended membrane. Neurophysiological studies and simplified optical models suggest that facial pits detect thermal radiation and form an image that is combined with visual input in the optic tectum to form a single multispectral image. External pit anatomy varies markedly among taxonomic groups. However, optical function depends on unknown internal anatomy. Therefore, we developed methods for relating anatomy to optical performance. To illustrate, we constructed detailed anatomical models of the internal anatomy of the facial pits of four individuals of four pitviper species using X-ray tomography sections of fresh material. We used these models to define the point spread function, i.e. the distribution of radiation from a point source over the pit membrane, for each species. We then used optical physics, heat transfer physics and computational image processing to define the thermal image formed on the pit membrane for each species. Our computed pit membrane images are consistent with behavioral observations if the sensitivity of membrane receptors equals the most sensitive (*ca.* 0.001°C) laboratory estimates. Vignetting (variation in optical aperture size with view angle) and differences between body and environmental temperatures can create temperature variation across the membrane that greatly exceeds image temperature contrasts, potentially impairing imaging. Spread functions plotted *versus* source point azimuth and elevation show distinct patterns that suggest new research directions into the relationships among the optical anatomy, ecology, behavior and sensory neurophysiology of pitvipers.**

Supplementary material available online at http://jeb.biologists.org/cgi/content/full/215/15/2621/DC1

## INTRODUCTION

The facial (loreal) pits of pitvipers (Viperidae: Crotalinae) provide a quasi-visual sense that detects thermal radiation (5–30 μm) rather than visual radiation (0.38–0.75 μm). The facial pit consists of a flask-shaped cavity divided into an inner and outer chamber by a suspended sensory membrane. A two-way exchange of thermal radiation through the pit aperture between source points and the pit membrane results in a temperature variation of *ca.* 0.1°C over the membrane (Bakken and Krochmal, 2007; de Cock Buning, 1984; Otto, 1972). Warm receptors in the pit membrane have a largely phasic/accommodative response, and primarily detect temperature contrasts (Bullock and Diecke, 1956; Van Dyke and Grace, 2010). Sensory output is transmitted to the brain *via* the trigeminal nerve (Lynn, 1931). Behaviorally, the facial pit appears to function as an 'eye' because it can compensate for visual deprivation (Kardong and Berkhoudt, 1999; Kardong and Mackessy, 1991). It aids prey acquisition (Bullock and Diecke, 1956; Clarke et al., 1996; de Cock Buning, 1983; Kardong, 1986; Noble and Schmidt, 1937) and thermoregulation (Krochmal and Bakken, 2003; Krochmal et al., 2004). Proposed but untested functions include situational awareness and predator detection (Bullock and Barrett, 1968; Greene, 1992; Sexton et al., 1992).

The explicit hypotheses that the facial pit is an imaging system (Otto, 1972; Stanford and Hartline, 1980) and that pitvipers perceive a visual–thermal multispectral image (Newman and Hartline, 1982) are supported by reports that neural image processing (image sharpening) in the medulla improves the resolution of the thermal image (Stanford and Hartline, 1980), neurons in the optic tectum respond to both thermal and visual signals (Hartline et al., 1978), and a common pathway transmits thermal and visual information to the forebrain (Berson and Hartline, 1988). Further, reports of neurons responding to ipsilateral, contralateral and bilateral stimulation suggest binocular thermal stereopsis (Berson and Hartline, 1988; Goris and Terashima, 1973).

However, imaging analyses using highly simplified pit geometry (Bakken and Krochmal, 2007; de Cock Buning, 1984; Otto, 1972) indicate the angular resolution of the temperature contrast image on the pit membrane to be poor. Low resolution optical systems are affected by aliasing, the formation of an image with features not present in the source scene. This mismatch of thermal and visual image resolution likely complicates multispectral image formation. Also, stereoacuity and angular resolution are linked (Howard and Rogers, 1995b) such that low thermal resolution limits binocular stereopsis of thermal signals.

A necessary step to reconcile the apparently contradictory evidence from physical optics and neurophysiology is to accurately define the nature, limitations and variability of the temperature contrast images formed on the pit membrane of diverse species.

Optically, the facial pit is a chamber-type eye with pinhole optics. Because of the 3D geometry of the pit aperture defining the 'pinhole', the shape of the optical aperture varies greatly with view angle and anatomical details. In the absence of such information, prior studies (Bakken and Krochmal, 2007; de Cock Buning, 1984; Otto, 1972) assumed extremely generalized and simplified geometry.

Therefore, we here present an analytical method that adapts the generalized optical model of Bakken and Krochmal (Bakken and Krochmal, 2007) to generate detailed simulations of the images formed on the pit membrane in relation to the precise optical geometry of facial pits reconstructed from serial X-ray computed tomography (CT) sections (Ketcham and Carlson, 2001) of fresh material.

## MATERIALS AND METHODS
### Overview

The facial pit images are computed with an extended version of the procedures developed previously (Bakken and Krochmal, 2007). These are detailed below. Briefly, the environment is represented by a thermogram, mathematically an array (matrix) of source points of radiance $I(\mathbf{y})$ ($W\,m^{-2}\,sr^{-1}$), where $\mathbf{y}$=(azimuth, elevation) is a mathematical vector giving the angular coordinates of the source point. In an ideal (perfectly focused) imaging system, the radiance of a given point $I(\mathbf{y}_i)$ will be mapped as the irradiance $M(\mathbf{x}_i)$ ($W\,m^{-2}$) of a single corresponding image point (the 'conjugate image point'), which is assigned the same coordinates $\mathbf{x}_i=\mathbf{y}_i$. The ideal image thus defines the coordinate system $\mathbf{x}$ over the image plane.

Our notation follows current image processing conventions (e.g. Puetter et al., 2005). Italic symbols indicate scalar parameters; boldface symbols indicate vector parameters. The angular coordinates of source and conjugate image points are specified as the azimuth and elevation of the source point as seen from the center of the pit, measured relative to the parasagittal and parapalatal planes. The use of angular coordinates is standard in geometric optics and results in size-independent calculations in which geometric similarity gives similar results.

The image formation process is shown as a schematic diagram in supplementary material Fig. S1. In a real optical system, radiation from a single source point $\mathbf{y}_i$ is spread over an area on the image plane surrounding the conjugate image point, $\mathbf{x}_i$. This area is called the point spread function. Specifically, radiation from a source point at $\mathbf{y}_i$ strikes the facial pit membrane if it passes through the pit aperture and not otherwise. Thermal radiation at 27°C (300K) peaks around 10μm, and thus diffraction significantly affects only the outer 2% (1st order fringe) of the diameter of the point spread function for a 1.5mm diameter pit aperture, 3mm from the membrane. Consequently, the source point can be considered to irradiate the spread function uniformly. The point spread function is therefore defined by a 4D matrix $P(\mathbf{x},\mathbf{y})$ with $P(\mathbf{x}_i,\mathbf{y}_j)=1$ if radiation emitted from a point at $\mathbf{y}_j$ can reach an image point at angular coordinates $\mathbf{x}_i$ on the pit membrane, and 0 if not. The resulting image is an irradiance distribution on the pit membrane $M(\mathbf{x})$ ($W\,m^{-2}$), and is found by summing the contributions of each source point $\mathbf{y}$ to every image point $\mathbf{x}$:

$$M(\mathbf{x}) = \int P(\mathbf{x},\mathbf{y})\,I(\mathbf{y})\mathrm{d}\mathbf{y} \; . \tag{1}$$

The pit membrane also receives background irradiance $B(\mathbf{x})$ from the pit wall. This radiation primarily sets the average temperature of the membrane. Total irradiance falling on the pit membrane $M(\mathbf{x})+B(\mathbf{x})$, thermal radiation emitted from the membrane, and conductive and convective heat transfer processes result in an image consisting of a distribution of temperatures over the membrane $T(\mathbf{x})$ (K). This image is sampled by *ca*. 3000–4000 warm receptors

(Bullock and Diecke, 1956; Terashima and Goris, 1979), and receptor sensitivity determines the neural input image, $D(\mathbf{x})$. The system incorporates tonic, phasic and accommodative responses (Bullock and Diecke, 1956; Goris and Nomoto, 1967; Goris and Terashima, 1973), but primarily detects temperature contrast over the membrane rather than absolute temperature (Bullock and Barrett, 1968; Van Dyke and Grace, 2010). The effect of average membrane temperature on the neurophysiological processes creating temperature contrast sensitivity is not well known, but the facial pit appears to function well over the 15–35°C range of body temperatures experienced by some active pitvipers (Beaupre and Duvall, 1998; Bullock and Diecke, 1956).

### Facial pit anatomy

The external anatomy of the facial pit shows considerable interspecific variation (Fig. 1). However, the optical properties are determined by internal 3D anatomy. Thus, to see whether variation in internal facial pit anatomy has significant consequences for facial pit imaging, we obtained X-ray CT sections from individuals of four species with different external pit geometries. These were *Crotalus atrox* Baird and Girard 1853, *Crotalus horridus* Linnaeus 1758, *Crotalus o. oreganus* Holbrook 1840, and *Cryptelytrops albolabris* Gray 1842. Specimens were anesthetized and killed according to IACUC protocol 2-10-2006:GSB/SEC. The head of the snake was frozen and cut coronally to remove the portion of the head from just caudal to the eyes to the tip of the snout. The frozen specimen was then glued to an L-shaped piece of plastic with cyanoacrylate adhesive to facilitate handling. The pits were stained with tincture of iodine to make the pit membrane more radio dense for better definition during scanning. The specimens were packaged in dry ice and shipped to the High-Resolution X-ray Computed Tomography Facility at The University of Texas at Austin for scanning. Digital sections (1024×1024 pixels) were returned to Indiana State University for analysis. The magnification of the CT images was set so that the head nearly filled the circular image field to provide maximum detail (Fig. 2A).

Anatomical procedures are detailed elsewhere (Colayori, 2009). The X-ray CT images (Fig. 2A) were aligned and image contrast adjusted to resolve the pit membrane. Images were processed using NeuroLucida software (MicroBrightField, Williston, VT, USA). Features on each section were traced and a 3D representation of the whole snake head was generated using the NeuroLucida solid modeling module (Fig. 2B).

### Optical analysis

As noted above, the optical spread function is just the projection of the pit aperture (optical pupil) onto the pit membrane (image plane) from the source point $\mathbf{y}_j$ (supplementary material Fig. S1). There are no reflective or refractive elements, and diffraction is negligible (Molenaar, 1992). To define the spread function matrix $P(\mathbf{x},\mathbf{y})$, we added color-coded spheres of uniform diameter to the pit membrane in the 3D model, such that nearest neighbors were in tangent contact (Fig. 2B). Markers were indexed by color code and the X-ray CT contour on which they were positioned. The angular dimensions of the markers were determined from CT section passing through the center of the pit. We used NeuroLucida to rotate the 3D representation of the head and noted which markers were the last visible from each extreme. We then subtracted the rotation angle where the first marker became visible from the front from the rotation angle where the last marker was visible from the side. The angular dimensions of a marker were determined by dividing the difference angle by the number of visible markers on that section. For example, 19 markers on the
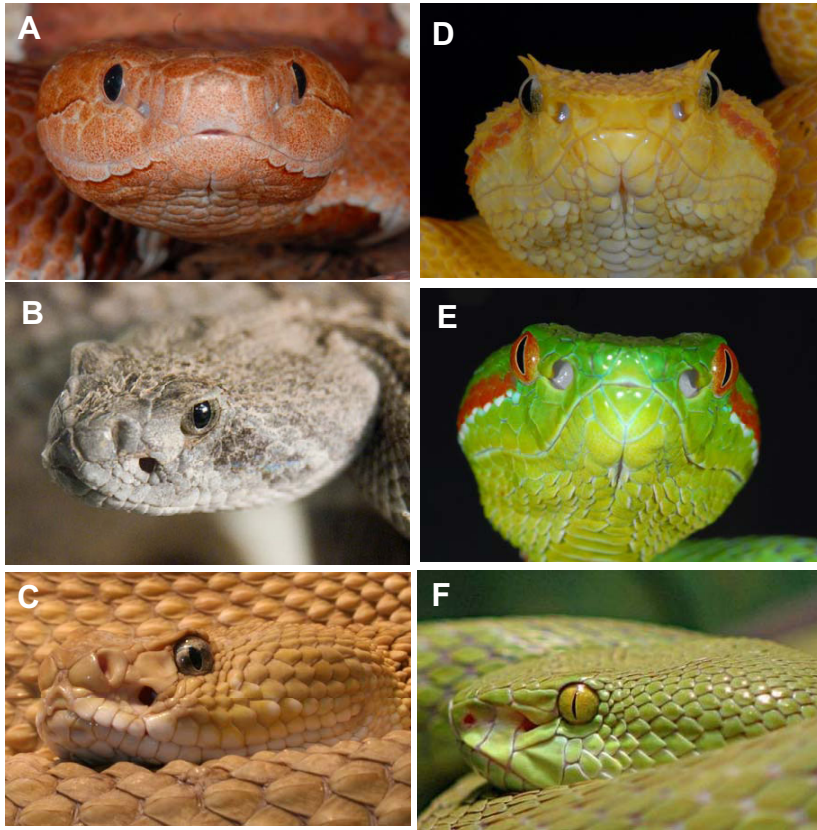
Fig. 1. Representative variation in external anatomy of the facial pit. (A) Copperhead, *Agkistrodon contortrix*. (B) Western diamondback rattlesnake, *Crotalus atrox*. (C) *Crotalus basiliscus*. (D) Eyelash viper, *Bothriechis schlegelii*. (E) *Viridovipera (Trimeresurus) gumprechti*. (F) White-lipped tree viper, *Cryptelytrops (Trimeresurus) albolabris*. Variation in the relative size of the facial pit opening is conspicuous (A *versus* E) but the optical significance depends entirely on the relationship to internal anatomy. The arboreal species (D,E,F) show a marked constriction or grooving of the face in front of the pits that appears to increase the sensory field overlap compared with the rounded nose of terrestrial species (A,B), although *C. basiliscus* (C) shows a similar feature with small grooves anterior to the pits. Photo credits: A,D,E, G. Westhoff; B, present study; C, H. Krisp; F, C. M. L. Burnett.

western diamondback rattlesnake membrane were visible while rotating the head through 95 deg, giving 95 deg/19=5 deg/marker. The dimensions of partly visible markers could be estimated to about 1/4 diameter, giving uncertainty in the marker count of <1/2 marker. This results in about 0.12 deg uncertainty in marker diameter (2.5%). Further, a small error in the estimated angular diameter of the markers resulted from variation in the distance from the center of the pit opening to the markers. This error had little effect over most of the membrane, but is large enough for source points directly in front of the snake that the angular dimensions of spread function may be overestimated by 5–10%. However, precision is more limited by the size of the markers used by NeuroLucida and, as will be evident later, an error of 5–12% in overall spread function dimensions has little effect on simulated membrane images.

The 4D spread function matrix $P(\mathbf{x},\mathbf{y})$ was defined by viewing the reconstructed head from source coordinates $\mathbf{y}_j$ spaced evenly at 10 deg in azimuth from –10 deg (contralateral) to 100 deg and 6 deg in elevation from +30 to –42 deg (Fig. 2B). The spread function for each $\mathbf{y}_j$, $P(\mathbf{x},\mathbf{y}_j)$, was then defined by superimposing the calibrated image of the markers visible through the pit aperture onto a scaled grid (Fig. 2B). This was then translated into an array of 1s and 0s in the corresponding cells of a Microsoft Excel 2002 spreadsheet (Microsoft, Redmond, WA, USA). Each cell in the spreadsheet corresponded to the 0.25 deg×0.25 deg pixels in the thermograms used as input images in our later analysis (Fig. 2C). A matrix element $P(\mathbf{x}_i,\mathbf{y}_j)$ located at $\mathbf{x}_i$ and viewed from $\mathbf{y}_j$ was set equal to 1 if radiation from the source pixel at $\mathbf{y}_j$ could reach it through the pit aperture, and 0 otherwise. The central marker visible through the pit aperture (pink, Fig. 2C) defined the optical conjugate of the source pixel at $\mathbf{y}_j$, and was assigned $\mathbf{x}_j=\mathbf{y}_j$. (Optical conjugates are the corresponding points of the source object and its ideal image, and are connected by the chief ray passing through the center of the optical pupil.)

Boundaries were adjusted when a fraction of the marker was visible to give a smooth representation of $P(\mathbf{x},\mathbf{y}_j)$. We assumed that the size and shape of the spread function varied little over a given 10 deg×6 deg grid cell, and assigned the same spread function $P(\mathbf{x},\mathbf{y}_j)$ to all $\mathbf{x}$ within that cell. For each species, we imported all 2D spread functions $P(\mathbf{x},\mathbf{y}_j)$ into Matlab and then assembled them into a 4D array representing $P(\mathbf{x},\mathbf{y})$.

### Computation of the facial pit membrane temperature distribution

Typically, thermograms are presented as an approximate surface temperature. The radiometric temperature of a source pixel, $T(\mathbf{y}_i)$ (K), corresponds to a radiance, $I(\mathbf{y}_i)$ (W m$^{-2}$ sr$^{-1}$), of:

$$I(\mathbf{y}_i) = \sigma\varepsilon T(\mathbf{y}_i)^4 / \pi . \qquad (2)$$

Here, the Stefan–Boltzmann constant $\sigma=5.67\times10^{-8}$ (W m$^{-2}$ K$^{-4}$) and $\varepsilon$ is the thermal emittance of the environmental surfaces, assumed to be $\varepsilon=1$ (typically, $\varepsilon>0.96$–0.98). The irradiance of a pixel on the pit membrane, $\Delta M(\mathbf{x}_i)$ (W m$^{-2}$) contributed by a pixel of temperature $T(\mathbf{y}_j)$ can be found using Eqn 2 (above) and eqn 4 from Bakken and Krochmal (Bakken and Krochmal, 2007) by noting that the solid angle of a 0.25 deg×0.25 deg pixel is $\Delta\omega=1.904\times10^{-5}$ sr:

$$\Delta M(\mathbf{x}_i) = I(\mathbf{y}_j)\ \Delta\omega = \sigma\varepsilon T(\mathbf{y}_j)^4\ \Delta\omega/\pi = 6.0602 \times 10^{-6}\ \sigma\varepsilon T(\mathbf{y}_j)^4 . \quad (3)$$

The facial pit membrane responds to temperature contrast $[T(\mathbf{x}_i)–T_{xr}]$, where $T_{xr}$ is an appropriate reference temperature (Bullock and Barrett, 1968; Van Dyke and Grace, 2010). Therefore, we converted irradiance to membrane temperature contrasts and incorporated heat transfer between the pit membrane and pit walls as previously [see eqns 4–9 of Bakken and Krochmal (Bakken and Krochmal, 2007)]. However, to accommodate pixel-wise computations, we used the solid angle of a pixel $\Delta\omega$ rather than the solid angle of the whole aperture. The
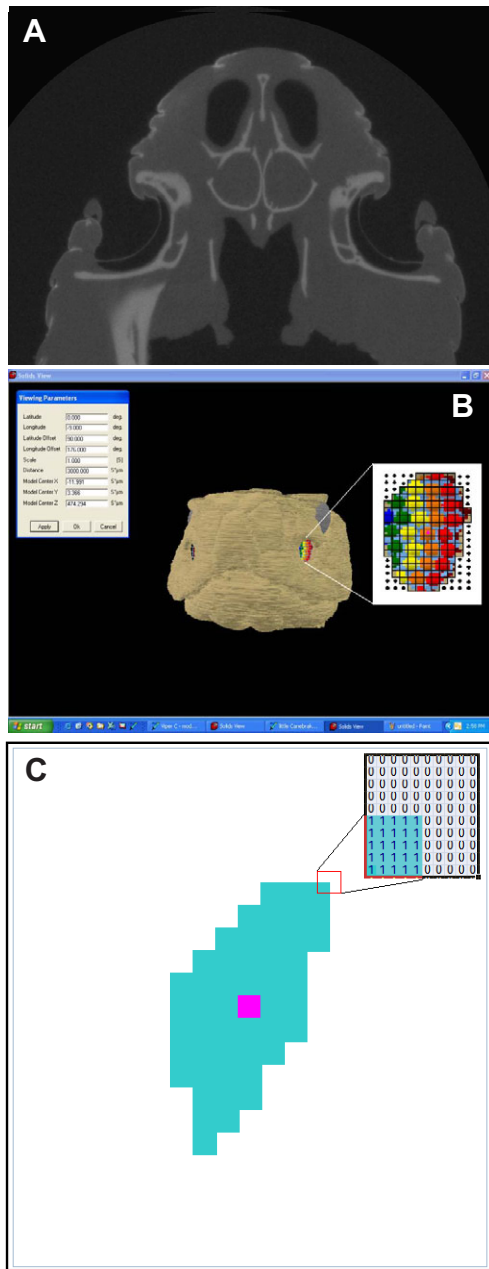
Fig. 2. Facial pit anatomy and measurement of optical spread functions. (A) Frontal plane X-ray computer tomography (CT) slice through the center of the facial pit of the *C. atrox* specimen. (B) 3D reconstruction of the head showing the pit membrane markers visible through the pit aperture. (C) Illustration of how the marker image is converted into the spread function matrix $P(\mathbf{x},\mathbf{y}_j)$ for a specific source point $\mathbf{y}_j$. The central marker shown in pink is the conjugate point defining $\mathbf{x}_j{=}\mathbf{y}_j$.

temperature contrast between two pixels on the membrane is then related to the temperature contrast between two source pixels by:

$$\left[T(\mathbf{x}_i)-T_{xr}\right] \approx \frac{6.0602\times10^{-6}}{\left[2+\left(\dfrac{k}{R}\right)\left(\dfrac{z+w}{zw}\right)\right]}\left[T(\mathbf{y}_i)-T_{yr}\right]. \qquad (4)$$

Here, $k$ is the thermal conductivity of air ($0.026\,\mathrm{W\,m^{-1}\,K^{-1}}$), $z$ (m) is the effective distance from the membrane to the wall of the outer (anterior) chamber, and $w$ (m) is the effective distance to the wall

of the inner (posterior) chamber. To present results in °C, we set $T_{yr}{=}273\,\mathrm{K}$ and linearized radiation heat transfer (Bakken, 1976) about snake body temperature, $T_b$. The linearized radiation heat transfer coefficient is then $R{=}4\sigma\varepsilon_m T_b^3$ ($\mathrm{W\,m^{-2}\,K^{-1}}$). We used published values of facial pit membrane absorptance (equal to emittance $\varepsilon_m$ at the same wavelength) for thermal radiation, $\alpha_m{>}0.5$ (Bullock and Diecke, 1956; Goris and Nomoto, 1967), and assumed facial pit dimensions of $z{=}0.002\,\mathrm{m}$, and $w{=}0.001\,\mathrm{m}$. As noted previously (Bakken and Krochmal, 2007), smaller pit dimensions will increase conductive heat loss and reduce image contrast, while larger pit dimensions will increase image contrast. To present the final image as temperature contrasts, we used the average temperature of the facial pit membrane for the reference temperature $T_{xr}$.

The dimensions of an image matrix $T(\mathbf{x})$ were set larger than the source thermogram dimensions such that the spread function matrix $P(\mathbf{x},\mathbf{y}_j)$ could be applied to marginal source thermogram pixels. Then, $M(\mathbf{x})$ is computed and converted to $T(\mathbf{x})$ using a finite-element equivalent of Eqn 1:

$$T(\mathbf{x}) = \sum_{\mathbf{y}}\left[T\left(\mathbf{y}\right)P(\mathbf{x},\mathbf{y})+T_b\overline{P}(\mathbf{x},\mathbf{y})\right] \qquad (5)$$

Here, $\overline{P}(\mathbf{x},\mathbf{y})$ is the 1's complement of $P(\mathbf{x},\mathbf{y})$, i.e. all 1s exchanged for 0s and *vice versa* to identify the area not receiving radiation from the environment. Thus, this term adds the portion of the background radiation $B(\mathbf{x})$ from the pit wall at temperature $T_b$ surrounding the aperture that is included in the $P(\mathbf{x},\mathbf{y}_i)$ matrix. Contributions to $B(\mathbf{x})$ from all other parts of the pit wall are essentially identical for all image pixels and therefore do not contribute to contrast, but do contribute to setting average membrane temperature within a fraction of a degree of head temperature.

Eqn 5 was evaluated by a Matlab script. For each thermogram pixel at $\mathbf{y}_j$ within the $10\,\mathrm{deg}{\times}6\,\mathrm{deg}$ grid cell, the spread function $P(\mathbf{x},\mathbf{y}_j)$ and its complement $\overline{P}(\mathbf{x},\mathbf{y}_j)$ were multiplied by the appropriate factors, centered on the conjugate image pixel $\mathbf{x}_j$ and summed to the image temperature distribution $T(\mathbf{x})$. After the contributions from all pixels in the source image to temperature contrast had been summed, the membrane image was converted to temperature contrast by subtracting the reference temperature $T_{xr}$ (defined as the average temperature of the computed image) and trimmed to the $60\,\mathrm{deg}{\times}80\,\mathrm{deg}$ dimensions of the source thermogram (for movies using doubled images, $60\,\mathrm{deg}{\times}160\,\mathrm{deg}$). To validate the script, we replicated the pit membrane temperature contrast images produced by a different computational method (Bakken and Krochmal, 2007) by using the circular spread functions from that study in the procedure reported here.

**Pit membrane images of field and laboratory scenes**

To compare the effect of variation in spread functions (Fig. 3) on imaging performance, we computed the irradiance image $M(\mathbf{x})$ and temperature contrast image $T(\mathbf{x})$. We defined realistic field scene arrays of surface temperatures $I(\mathbf{y})$ by using a radiometric FLIR PM 575 thermal imager (FLIR Systems, Portland, OR, USA) to obtain $60\,\mathrm{deg}{\times}80\,\mathrm{deg}$ (vertical×horizontal) thermograms or thermogram movies with $0.25\,\mathrm{deg}{\times}0.25\,\mathrm{deg}$ pixels. Temperature contrast resolution was 0.1°C with an absolute accuracy of 1–2°C.

We applied published estimates of the pit membrane temperature sensitivity (Bullock and Diecke, 1956) to estimate the neural input image $D(\mathbf{x})$ for each species studied. We used minimum estimates of heat loss from the pit membrane; higher heat loss rates (e.g. due to perfusion of the pit membrane) (Goris et al., 2000) result in a faster response, but require increased receptor temperature sensitivity as a
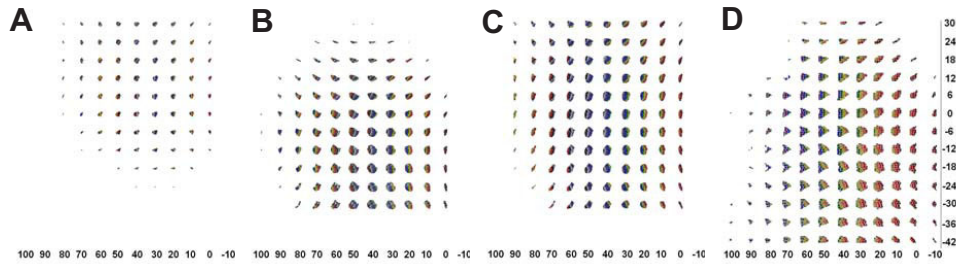
Fig. 3. Optical point spread functions for four pitviper species. (A) *Crotalus atrox*. (B) *Crotalus o. oreganus*. (C) *Crotalus horridus*. (D) *Cryptelytrops albolabris*. Spread functions (the area illuminated by radiation from a point source) are plotted in a 90 deg×90 deg cell as if projected onto the source scene viewed by the left pit. To give a representation of the variation in spread function over the pit membrane, we have used point sources spaced 6 deg in elevation and 10 deg in azimuth. Spread functions are arranged in an array by the coordinates of the point sources as indicated on the margin. Elevation is positive upward, and negative azimuth is contralateral. The data for *C. albolabris* extend to –42 deg; others to –30 deg. For all species, the individual point spread functions overlap greatly. Colored markers identify fixed points on the facial pit membrane and can be used to visualize the degree of overlap of the spread functions.

given stimulus creates a smaller membrane temperature change. The color scale steps correspond to a contrast of 0.001°C, equal to the most sensitive discrimination suggested in a neurophysiological study (Bullock and Diecke, 1956). For comparison of our results with published laboratory estimates of distances at which a mouse can be detected (Ebert and Westhoff, 2006; Goris et al., 2000; Kardong, 1986; Safer and Grace, 2004; Stanford and Hartline, 1984), we generated slow-frame 60 deg×160 deg thermographic source movies using Matlab scripts. These simulate, first, a high-temperature quasi-point source such as a soldering iron or cigarette (e.g. Goris et al., 2000; Stanford and Hartline, 1984) passing right to left in front of the snake. Second, we simulated BALB/c mice at various distances in a room temperature environment (e.g. Ebert and Westhoff, 2006; Kardong, 1986; Safer and Grace, 2004). The 'mice' are based on thermograms of live mice, and consist of moving disks 7.6°C warmer than a uniform 23°C background. The disks are sized to simulate the angular dimensions of a mouse at 20, 30, 50 and 75 cm.

## RESULTS AND DISCUSSION
### Optical spread function characteristics
The optical spread functions of our four specimens, projected onto the source scene as viewed by the left pit, are plotted in Fig. 3. Individual plots of spread functions $P(\mathbf{x}, \mathbf{y}_j)$ for a specific source point $\mathbf{y}_j$ are plotted in individual 90 deg×90 deg cells with **x** coordinates for the axes, while the individual $P(\mathbf{x}, \mathbf{y}_j)$ plots are arranged in an array by **y** coordinates to give an overall representation of the 4D spread function $P(\mathbf{x}, \mathbf{y})$. For all species, the individual point spread functions overlap greatly. It is evident from Fig. 3 that the shape and included solid angle of $P(\mathbf{x}, \mathbf{y})$ vary with source point coordinates **y**. Spread functions for a given source coordinate **y** vary markedly among the four species. Consequently, the overall patterns of the spread function plots differ in interesting ways.

First, for all four species the sensory fields are centered on 40–50 deg azimuth (Fig. 3). However, the elevation of the center of the sensory field varies. The sensory fields of *C. atrox* (Fig. 3A) are elevated 15–20 deg above horizontal. The sensory fields of *C. o. oreganus* (Fig. 3B) are depressed 15–20 deg. Sensory fields of *C. horridus* (Fig. 3C) are horizontal. Sensory fields of *C. albolabris* (Fig. 3D) are depressed 20–30 deg below horizontal.

Second, the forward overlap of the sensory fields of the three rattlesnakes is less than 10 deg, while the forward overlap of the arboreal Southeast Asian *C. albolabris* exceeds 20 deg (Fig. 3A,D). Compared with typical rattlesnakes (Fig. 1B,C), the snout of *C.*

*albolabris* (Fig. 1F) is distinctively reduced in front of the pits creating a 'scooped out' appearance that permits this overlap. Interestingly, this morphology is shared by other Asian tree vipers (Fig. 1E) (see also Gumprecht et al., 2004), and by the geographically and phylogenetically disjunct (Parkinson, 1999) arboreal neotropical pitviper *Bothriechis schlegelii* (Fig. 1D). This sensory field overlap supports the stereopsis hypothesis (Berson and Hartline, 1988; Goris and Terashima, 1973) based on the presence of neurons responding to ipsilateral and contralateral facial pit input.

However, the functional significance of overlap in visual sensory fields is controversial and need not indicate stereo vision (Heesey, 2009; Howard and Rogers, 1995a). Hypotheses include (1) stereopsis aiding 3D arboreal movements (Berson and Hartline, 1988; Collins, 1921; Goris and Terashima, 1973), (2) stereopsis aiding cryptic prey detection (Howard and Rogers, 1995a), and (3) the $\sqrt{2}$ gain in sensitivity obtained by summing two noisy inputs (Campbell and Green, 1965). These are compatible hypotheses for thermal radiation imaging in these arboreal species. Similarly, thermal imaging with stereopsis may benefit either movement within the arboreal environment on moonless nights or the detection of low thermal contrast prey such as anurans.

Third, *C. atrox* has spread functions that are markedly smaller than those of the other three species (Fig. 3). The significance is unclear, but it has been noted (Bakken and Krochmal, 2007) that the facial pit apertures defining $P(\mathbf{x}, \mathbf{y})$ generally appear larger than optimal because large spread functions reduce angular resolution but provide no compensating increase in the image irradiance contrast for small or distant source objects that subtend a solid angle smaller than the solid angle of the pit aperture.

### Image-forming characteristics
Laboratory environments with uniform thermal background
Supplementary material Movie 1 compares the pit membrane images for the two most extreme facial pit anatomies, *C. atrox* and *C. albolabris*. The 60 deg×160 deg source thermograms first simulate a high-temperature quasi-point source (e.g. Goris et al., 2000; Stanford and Hartline, 1984) passing right to left in front of the snake. As expected, the image of the quasi-point source is distinct and approximates the spread function.

The quasi-point source is followed by simulated mice. We recorded thermograms of an adult BALB/c mouse in a typical lab environment at 23°C and measured the area and average temperature with IRwin Research software (FLIR Systems, Portland, OR, USA).
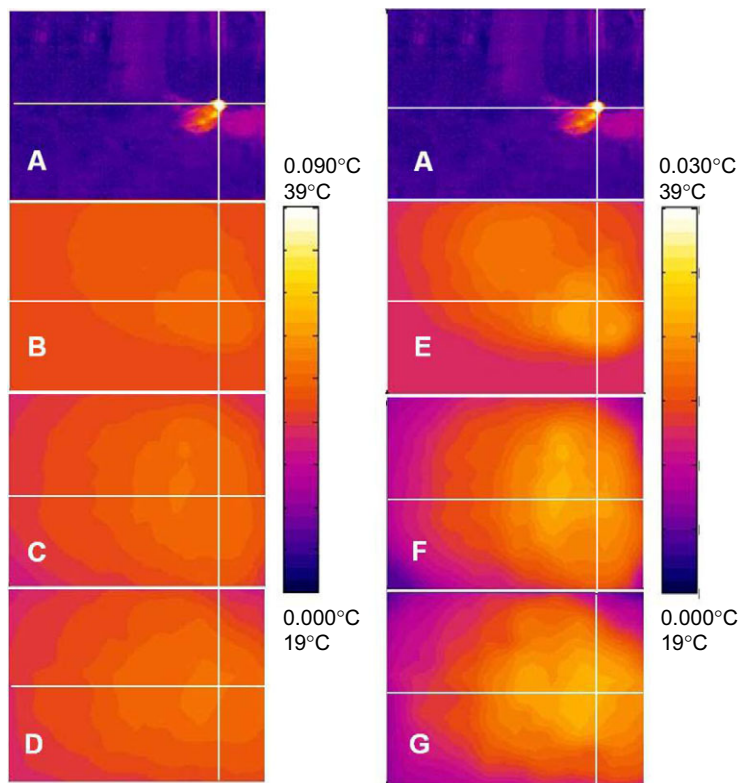
Fig. 4. Comparisons of computed temperature distributions on facial pit membranes for three pitviper species. (A) Source scene of a bird, *Cardinalis cardinalis*, in a woodlot, temperature range 19–39°C. (B–D) Facial pit membrane temperature distribution for (B) *C. atrox*, (C) *C. horridus* and (D) *C. albolabris*, all with temperature range 0.000–0.090°C and 0.003°C color steps to simulate 0.003°C sensitivity. (E–G) Same as B–D, but with 0.001°C color steps to simulate 0.001°C sensitivity. Results for *C. oreganus* are similar to those for *C. horridus*. The color scale legend gives the temperature range for the pit membrane images (B–G) above and for the source scene (A) below. The bird, horizontal log and tree are arguably distinguishable in the *C. atrox* pit membrane image with 0.001°C sensitivity, while assuming 0.003°C sensitivity or the larger spread functions for the other species results in uninterpretable images. The reference crosshairs are centered on the bird's head to aid comparison.

Based on these data, we used Matlab script to generate 'mice' consisting of moving disks 7.6°C warmer than a uniform 23°C background, sized to simulate the total area of a mouse at 20, 30, 50 and 75 cm. These movies simulate the membrane image of a mouse or mouse-like targets as used in behavioral studies (e.g. Ebert and Westhoff, 2006; Kardong, 1986; Safer and Grace, 2004).

Such studies have been used to estimate the threshold contrast sensitivity. Bullock and Diecke found a strong enough response to changes of 0.0025°C in water flowing over the membrane to extrapolate to a threshold receptor sensitivity 0.001°C (Bullock and Diecke, 1956). To incorporate this result, we represent a membrane temperature change of 0.001°C as one color step in the image. With this presentation, the 'mouse' is clearly evident at 20 cm. Because the stimulus does not fill the pit aperture, the images at 30 and 50 cm are weaker, indicated by fewer 0.001°C steps above background temperature. At 75 cm no image is produced. This is roughly in agreement with the finding that *C. atrox* is able to detect a mouse-like stimulus at a distance of no more than 80 cm (Ebert and Westhoff, 2006). However, using the more conservative assumption of 0.003°C sensitivity (Barrett et al., 1970), corresponding to three color steps in the image, the 'mouse' is visible only at 20 cm. Consequently, our results, in combination with those of Ebert and Westhoff (Ebert and Westhoff, 2006), suggest that membrane receptor sensitivity is approximately equal to the 0.001°C threshold proposed by Bullock and Diecke (Bullock and Diecke, 1956). This appears remarkable, but our computations are conservative as regards sensitivity estimates. Heat transfer computations in Eqn 4 incorporate only thermal radiation and conduction through stagnant air inside the facial pit. Including air convection within the pit chambers or convective–conductive heat flow within the membrane would give lower temperature contrasts and thus require a threshold sensitivity of <0.001°C to explain the results of Ebert and Westhoff (Ebert and Westhoff, 2006).

Comparison of the *C. albolabris* and *C. atrox* pit membrane images shows that the former has a somewhat stronger signal as the mouse passes directly in front of the nose due to the large forward and contralateral spread functions, which might be further enhanced by summing the overlapping left and right sensory fields (not simulated). The overall effect of variation in aperture size on the distance at which a mouse-like target can be detected is small, with association between stronger signal and large pit apertures evident only at close range, because the target usually does not fill the pit aperture (Bakken and Krochmal, 2007).

### Field environments

Natural habitats are spatially complex. Consequently, generalizing laboratory studies using simple sources against a thermally uniform background may be misleading. Therefore, we computed membrane images of 60 deg×80 deg outdoor scenes including a prey item (a bird, Fig. 4A). The pit membrane of *C. atrox* receives an arguably recognizable image (Fig. 4B and 4E, best viewed online), with brighter areas corresponding to the tree trunk and fallen branch and the brightest area to the bird. However, large spread functions weight large areas of moderate thermal contrast as heavily as high contrast objects smaller than the spread function. Thus, for *C. horridus* (Fig. 4C and 4F) and *C. albolabris* (Fig. 4D and 4G), the most intense point in the image is displaced away from the most intense source area because radiation from the bird and warm background objects have merged into a comparatively intense, but aliased and largely un-interpretable image. Movement, particularly if combined with a phasic response (Goris and Terashima, 1973), makes it easier to distinguish prey from background features. However, it does not enhance signal strength, as is evident in supplementary material Movies 2–6. These 60 deg×160 deg thermal movies show a mouse passing *ca*. 20–30 cm in front of the 'snake', and were generated by adding a reflected 60 deg×80 deg frame of the same scene taken
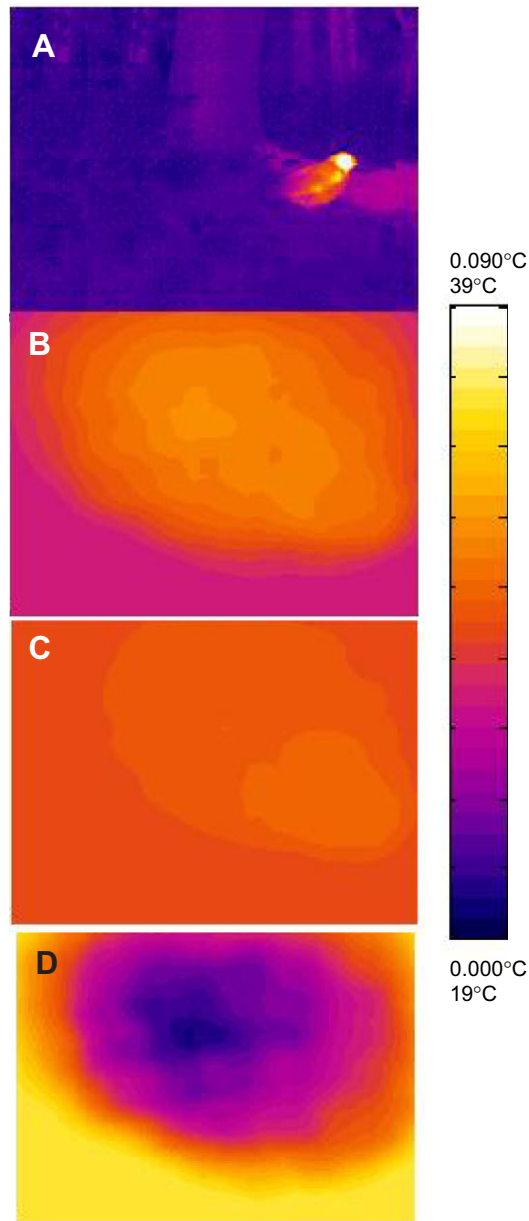
characteristics (Bullock and Diecke, 1956; Stanford and Hartline, 1984), functions over a wide range of active body temperatures. However, the dynamic contrast range may be limited (estimated to be $100\times$ minimum sensitivity) (Bullock and Diecke, 1956). This may limit performance when body temperature differs from ambient temperature, because background radiation from the walls of the facial pit, together with peripheral decreases in the size of the spread function, result in vignetting (Fig. 5). Depending on the dynamic range of the receptors, either facial pit function is impaired until the snake reaches steady state with its thermal environment or some combination of localized phasic and/or accommodative receptor response and CNS processing (Stanford and Hartline, 1984) corrects for the variation in average temperature.

## CONCLUSIONS

We have shown that 3D anatomical reconstruction, optics, heat transfer physics and image processing methods can be combined to create representations of the thermal image on the facial pit membrane. The results are in rough agreement with neurophysiological (Bullock and Diecke, 1956) and behavioral (Ebert and Westhoff, 2006) estimates of membrane sensitivity. Our comparison of spread functions and image formation of both laboratory and outdoor scenes for our four specimens indicates that image formation is significantly affected by the detailed geometry of the facial pit.

Our method opens a new approach to a variety of physiological, behavioral and ecological studies. First, the poor optical resolution of the membrane image results in aliasing in our pit membrane image simulations, but this may not characterize overall performance because CNS image sharpening has been demonstrated (Stanford and Hartline, 1984). The mechanisms for facial pit image sharpening (Stanford and Hartline, 1984) need renewed attention utilizing modern neurophysiological techniques.

Detection threshold, contrast sensitivity and dynamic range need continuing attention using both behavioral and neurophysiological assays. First, image sharpening is sensitive to the dynamic range in a blurred image (Gonzalez and Wintz, 1977). Second, as snakes are ectotherms, body temperature needs to be an experimental variable. We have demonstrated that differences of 5–15°C between body and ambient surface temperatures cause vignetting that challenges accommodation to background signals. Also, body temperature may affect overall contrast sensitivity. While molecular channels responding above 28°C have been identified in facial pit innervation (Gracheva et al., 2010), facial pits are reported to function well at body temperatures below 20°C (Bullock and Diecke, 1956). Thus, other molecular channels and thermal processes including perfusion changes (Goris et al., 2000) and metabolic heat generation in the mitochondria-packed sensory endings (Bleichmar and De Robertis, 1962) need detailed attention.

Body size may affect threshold sensitivity. We previously found that smaller pit cavities would have greater heat loss by conduction through air and thus be less sensitive (Bakken and Krochmal, 2007).

Our results indicate that phylogenetic analysis might also be rewarding. A particularly interesting set of questions relates to the evolutionary ecology of the facial pit, particularly whether variation in facial pit anatomy is associated with/adapted to habitat. Possible functional relationships between ecology and anatomical features such as aperture size and the vertical orientation and forward overlap of the optical axes need to be tested by ecological and behavioral studies. Studies should include accurate determination of normal head position relative to relevant environmental objects during foraging, resting, defensive posture and movement. Also, it is worth



Fig. 5. Comparisons of computed temperature distributions on facial pit membranes of *C. atrox* for three body temperatures. (A) Source scene of a bird, *C. cardinalis*, in a woodlot. (B–D) Facial pit membrane temperature distribution with body temperatures of: (B) 16°C, (C) 20°C and (D) 36°C. Temperature scale as in Fig. 2, with color steps assuming 0.003°C sensitivity to avoid image saturation by the large temperature variation caused by background radiation from the pit walls.

just before the mouse appeared to give a 60 deg×160 deg doubled frame. To give the appearance of a mouse crossing in front of the snake, the frames were then reflected horizontally and appended in reverse order. Supplementary material Movie 2 compares the full thermal image (tonic response) for *C. atrox* and *C. albolabris*. Supplementary material Movies 3–6 compare tonic and 20% tonic plus 80% phasic responses for each of the four study species.

### Variation in body temperature

The facial pit membrane is close to body (anterior portion of the head) temperature and, because of its phasic and accommodative

investigating whether larger-than-optimal apertures might be explained as serving to increase sensitivity in conjunction with neural summation of multiple membrane receptors (Stanford and Hartline, 1984). This mechanism is known to increase sensitivity in the visual systems of nocturnal species (Hess et al., 1990).

Finally, our methods allow investigation of a variety of interesting questions in behavioral ecology. For example, is the ability to detect prey items affected by background clutter and, if so, are ambush sites selected to minimize thermal background clutter? Is imaging contrast sensitivity affected by wind-created convection within the outer pit cavity (Bakken and Krochmal, 2007) and, if so, are windy sites avoided?

All of these questions can be approached using our methods to generate pit membrane images that can be compared with neurophysiological results and demonstrated behavioral capabilities in laboratory and field studies.

## LIST OF SYMBOLS AND ABBREVIATIONS

| | |
|---|---|
| $B(\mathbf{x})$ | background irradiance at image point $\mathbf{x}$ due to thermal radiation from the pit wall $(\mathrm{W\,m^{-2}})$ |
| $D(\mathbf{x})$ | neural input image |
| $I(\mathbf{y})$ | radiance of source point at coordinates $\mathbf{y}$ $(\mathrm{W\,m^{-2}\,sr^{-1}})$ |
| $k$ | thermal conductivity of air, $k=0.026$ $(\mathrm{W\,m^{-1}\,K^{-1}})$ |
| $\Delta M(\mathbf{x})$ | contribution to irradiance at image point $\mathbf{x}$ due to source pixel at $\mathbf{y}$ $(\mathrm{W\,m^{-2}})$ |
| $M(\mathbf{x})$ | irradiance at image point $\mathbf{x}$ $(\mathrm{W\,m^{-2}})$ |
| $P(\mathbf{x},\mathbf{y})$ | point spread function for source coordinate $\mathbf{y}$ and image coordinate $\mathbf{x}$, elements 1 or 0 (dimensionless) |
| $\bar{P}(\mathbf{x},\mathbf{y})$ | 1's complement of the point spread function (1s replaced by 0s and *vice versa*) for source coordinate $\mathbf{y}$ and image coordinate $\mathbf{x}$ |
| $R$ | equivalent conductance due to thermal radiation, $R=4\sigma\varepsilon_\mathrm{m}T_\mathrm{b}^3$ $(\mathrm{W\,m^{-2}\,K^{-1}})$ |
| $T_\mathrm{b}$ | snake body (pit wall) temperature (°C or K) |
| $T(\mathbf{x})$ | temperature of the facial pit membrane at coordinate $\mathbf{x}$ (°C or K) |
| $T_{xr}$ | reference temperature |
| $T(\mathbf{y})$ | temperature of the source at coordinate $\mathbf{y}$ (°C or K) |
| $w$ | effective distance from membrane to the wall of the inner (posterior) chamber (m) |
| $\mathbf{x}$ | vector coordinates (azimuth and elevation) of a general point or pixel on the facial pit membrane (angular deg) |
| $\mathbf{x}_i$ | vector coordinates (azimuth and elevation) of a specific point or pixel on the facial pit membrane (angular deg) |
| $\mathbf{x}_j, \mathbf{y}_j$ | coordinates of a pair of conjugate source and image points or pixels (angular deg) |
| $\mathbf{y}$ | vector coordinates (azimuth and elevation) of a general source point or pixel (angular deg) |
| $\mathbf{y}_i$ | vector azimuth and elevation of a specific source point or pixel (angular deg) |
| $z$ | effective distance from membrane to the wall of the outer (anterior) chamber (m) |
| $\alpha_\mathrm{m}$ | average absorptance of facial pit membrane for thermal radiation *ca.* 0.5 (dimensionless) |
| $\Delta\omega$ | solid angle of source pixel (sr) |
| $\varepsilon$ | emittance of source surface for thermal infrared radiation, assumed to be 1 (range 0.96–0.98 for natural surfaces) (dimensionless) |
| $\varepsilon_\mathrm{m}$ | average emittance of facial pit membrane for thermal infrared radiation (equal to absorptance at the same wavelengths, $\alpha_\mathrm{m}$) *ca.* 0.5 (dimensionless) |
| $\sigma$ | Stefan–Boltzmann constant, $5.67\times10^{-8}$ $(\mathrm{W\,m^{-2}\,K^{-4}})$ |

## REFERENCES

**Bakken, G. S.** (1976). A heat transfer analysis of animals: unifying concepts and the application of metabolism chamber data to field ecology. *J. Theor. Biol.* **60**, 337-384.

**Bakken, G. S. and Krochmal, A. R.** (2007). The imaging properties and sensitivity of the facial pits of pitvipers as determined by optical and heat-transfer analysis. *J. Exp. Biol.* **210**, 2801-2810.

**Barrett, R., Maderson, P. F. A. and Meszler, R. M.** (1970). The pit organ of snakes. In *Biology of the Reptilia*, Vol. 2 (ed. C. Gans), pp. 277-300. New York: Academic Press.

**Beaupre, S. J. and Duvall, D.** (1998). Variation in oxygen consumption of the western diamondback rattlesnake (*Crotalus atrox*): implications for sexual size dimorphism. *J. Comp. Physiol. B* **168**, 497-506.

**Berson, D. M. and Hartline, P. H.** (1988). A tecto-rotundo-telencephalic pathway in the rattlesnake: evidence for a forebrain representation of the infrared sense. *J. Neurosci.* **8**, 1074-1088.

**Bleichmar, H. and De Robertis, E.** (1962). Submicroscopic morphology of the infrared receptor of pit vipers. *Z. Zellforsch. Mikrosk. Anat.* **56**, 748-761.

**Bullock, T. H. and Barrett, R.** (1968). Radiant heat reception in snakes. *Commun. Behav. Biol.* **1**, 19-29.

**Bullock, T. H. and Diecke, F. P. J.** (1956). Properties of an infra-red receptor. *J. Physiol.* **134**, 47-87.

**Campbell, F. W. and Green, D. G.** (1965). Monocular versus binocular visual acuity. *Nature* **208**, 191-192.

**Clarke, J. A., Chopko, J. T. and Mackessy, S. P.** (1996). The effect of moonlight on activity patterns of adult and juvenile prairie rattlesnakes (*Crotalus viridis viridis*). *J. Herpetol.* **30**, 192-197.

**Colayori, S. E.** (2009). Anatomy and infrared imaging properties of the facial pits of pitvipers. MS thesis, Department of Biology, Indiana State University, Terre Haute, IN, 54pp.

**Collins, E. T.** (1921). Changes in the visual organs correlated with the adoption of arboreal life and with the assumption of the erect posture. *Trans. Ophthal. Soc. UK* **41**, 10-90.

**de Cock Buning, T.** (1983). Thermal sensitivity as a specialization for prey capture and feeding in snakes. *Am. Zool.* **23**, 363-375.

**de Cock Buning, T.** (1984). A theoretical approach to the heat sensitive pit organs of snakes. *J. Theor. Biol.* **111**, 509-529.

**Ebert, J. and Westhoff, G.** (2006). Behavioural examination of the infrared sensitivity of rattlesnakes (Crotalus atrox). *J. Comp. Physiol. A* **192**, 941-947.

**Gonzalez, R. C. and Wintz, P.** (1977). *Digital Image Processing*. Reading, MA: Addison-Wesley.

**Goris, R. C. and Nomoto, M.** (1967). Infrared reception in oriental Crotaline snakes. *Comp. Biochem. Physiol.* **23**, 879-892.

**Goris, R. C. and Terashima, S. I.** (1973). Central response to infra-red stimulation of the pit receptors in a crotaline snake, *Trimeresurus flavoviridis*. *J. Exp. Biol.* **58**, 59-76.

**Goris, R., Nakano, M., Atobe, Y., Kadota, T., Funakoshi, K., Hisajima, T. and Kishida, R.** (2000). Nervous control of blood flow microkinetics in the infrared organs of pit vipers. *Auton. Neurosci.* **84**, 98-106.

**Gracheva, E. O., Ingolia, N. T., Kelly, Y. M., Cordero-Morales, J. F., Hollopeter, G., Chesler, A. T., Sánchez, E. E., Perez, J. C., Weissman, J. S. and Julius, D.** (2010). Molecular basis of infrared detection by snakes. *Nature* **464**, 1006-1011.

**Greene, H. W.** (1992). The ecological and behavioral context for pitviper evolution. In *Biology of the Pitvipers* (ed. J. A. Campbell and E. D. Brodie, Jr), pp. 107-117. Tyler, TX: Selva.

**Gumprecht, A., Tillack, F., Orlov, N. L., Captain, A. and Ryabov, S.** (2004). *Asian Pitvipers*. Berlin: Geitje Books.

**Hartline, P. H., Kass, L. and Loop, M. S.** (1978). Merging of modalities in the optic tectum: infrared and visual integration in rattlesnakes. *Science* **199**, 1225-1229.

**Heesey, C. P.** (2009). Seeing in stereo: the ecology and evolution of primate binocular vision and stereopsis. *Evol. Anthropol.* **18**, 21-35.

**Hess, R. F., Sharpe, L. T. and Nordby, K.** (1990). *Night Vision: Basic, Clinical, and Applied Aspects*. Oxford, UK: Oxford University Press.

**Howard, I. P. and Rogers, B. J.** (1995a). Binocular and stereoscopic vision in animals. In *Binocular Vision and Stereopsis* (ed. N. J. Mackintosh, D. Schacter, A. Treisman, J. L. McGaugh, T. Shallice and L. Weiskrantz), pp. 645-657. New York: Oxford University Press.

**Howard, I. P. and Rogers, B. J.** (1995b). The limits of stereoscopic vision. In *Binocular Vision and Stereopsis* (ed. N. J. Mackintosh, D. Schacter, A. Treisman, J. L. McGaugh, T. Shallice and L. Weiskrantz), pp. 149-194. New York: Oxford.

**Kardong, K. V.** (1986). Predatory strike behavior of the rattlesnake, *Crotalus viridis oreganus*. *J. Comp. Psychol.* **100**, 304-314.

**Kardong, K. V. and Berkhoudt, H.** (1999). Rattlesnake hunting behavior: correlations between plasticity of predatory performance and neuroanatomy. *Brain Behav. Evol.* **53**, 20-28.

**Kardong, K. V. and Mackessy, S. P.** (1991). The strike behavior of a congenitally blind rattlesnake. *J. Herpetol.* **25**, 208-211.

**Ketcham, R. A. and Carlson, W. D.** (2001). Acquisition, optimization and interpretation of X-ray computed tomographic imagery: applications to the geosciences. *Comput. Geosci.* **27**, 381-400.

**Krochmal, A. R. and Bakken, G. S.** (2003). Thermoregulation is the pits: use of thermal radiation for retreat site selection by rattlesnakes. *J. Exp. Biol.* **206**, 2539-2545.

**Krochmal, A. R., Bakken, G. S. and LaDuc, T. J.** (2004). Heat in evolution's kitchen: evolutionary perspectives on the functions and origin of the facial pit of pitvipers (Viperidae: Crotalinae). *J. Exp. Biol.* **207**, 4231-4238.

**Lynn, W. G.** (1931). The structure and function of the facial pit of the pit viper. *Am. J. Anat.* **49**, 97-139.

**Molenaar, G. J.** (1992). Anatomy and physiology of infrared sensitivity of snakes. In *Biology of the Reptilia, Neurology C: Sensorimotor Integration*, Vol. 17 (ed. C. Gans and P. S. Ulinski), pp. 367-453. Chicago, IL: University of Chicago Press.

**Newman, E. A. and Hartline, P. H.** (1982). The infrared 'vision' of snakes. *Sci. Am.* **246**, 116-127.

**Noble, G. K. and Schmidt, A.** (1937). The structure and function of the facial and labial pits of snakes. *Proc. Am. Philos. Soc.* **77**, 263-288.

**Otto, J.** (1972). Das Grubenorgan, ein biologisches System zur Abbildung von Infrarotstrahlern. *Biol. Cybern.* **10**, 103-106.

**Parkinson, C. L.** (1999). Molecular systematics and biogeographical history of pitvipers as deterined by mitochondrial ribosomal DNA sequences. *Copeia* **1999**, 576-586.

**Puetter, R. C., Gosnell, T. R. and Yahil, A.** (2005). Digital imaging reconstruction: deblurring and denoising. *Annu. Rev. Astron. Astrophys.* **43**, 139-194.

**Safer, A. B. and Grace, M. S.** (2004). Infrared imaging in vipers: differential responses of crotaline and viperine snakes to paired thermal targets. *Behav. Brain Res.* **154**, 55-61.

**Sexton, O. J., Jacobson, P. and Bramble, J. E.** (1992). Geographic variation associated with some activities associated with hibernation in Nearctic pitvipers. In *Biology of the Pitvipers* (ed. J. A. Campbell and E. D. Brodie, Jr), pp. 337-345. Tyler, TX: Selva.

**Stanford, L. R. and Hartline, P. H.** (1980). Spatial sharpening by second-order trigeminal neurons in crotaline infrared system. *Brain Res.* **185**, 115-123.

**Stanford, L. R. and Hartline, P. H.** (1984). Spatial and temporal integration in primary trigeminal nucleus of rattlesnake infrared system. *J. Neurophysiol.* **51**, 1077-1090.

**Terashima, S. and Goris, R. C.** (1979). Receptive areas of primary infrared afferent neurons in crotaline snakes. *Neuroscience* **4**, 1137-1144.

**Van Dyke, J. U. and Grace, M. S.** (2010). The role of thermal contrast in infrared-based defensive targeting by the copperhead, *Agkistrodon contortrix. Anim. Behav.* **79**, 993-999.